# Evidence of magnetism-induced topological protection in the axion insulator candidate EuSn$_2$P$_2$

Gian Marco Pierantozzi[a,1] [ID], Alessandro De Vita[a,b,1] [ID], Chiara Bigi[a], Xin Gui[c], Hung-Ju Tien[d], Debashis Mondal[a,e], Federico Mazzola[a], Jun Fujii[a], Ivana Vobornik[a], Giovanni Vinai[a], Alessandro Sala[a], Cristina Africh[a], Tien-Lin Lee[f], Giorgio Rossi[a,b] [ID], Tay-Rong Chang[d,g,h] [ID], Weiwei Xie[i] [ID], Robert J. Cava[c,2], and Giancarlo Panaccione[a]

[a]Istituto Officina dei Materiali, Consiglio Nazionale delle Ricerche, Trieste I-34149, Italy; [b]Dipartimento di Fisica, University of Milano, Milano I-20133, Italy; [c]Department of Chemistry, Princeton University, Princeton, NJ 08544; [d]Department of Physics, National Cheng Kung University, Tainan 701, Taiwan; [e]International Centre for Theoretical Physics, Trieste I-34100, Italy; [f]Diamond Light Source, Harwell Science and Innovation Campus, Didcot OX11 0DE, United Kingdom; [g]Center for Quantum Frontiers of Research and Technology, Tainan 701, Taiwan; [h]Physics Division, National Center for Theoretical Sciences, National Taiwan University, Taipei 10617, Taiwan; and [i]Department of Chemistry and Chemical Biology, Rutgers University, Piscataway, NJ 08854

We unravel the interplay of topological properties and the layered (anti)ferromagnetic ordering in EuSn$_2$P$_2$, using spin and chemical selective electron and X-ray spectroscopies supported by first-principle calculations. We reveal the presence of in-plane long-range ferromagnetic order triggering topological invariants and resulting in the multiple protection of topological Dirac states. We provide clear evidence that layer-dependent spin-momentum locking coexists with ferromagnetism in this material, a cohabitation that promotes EuSn$_2$P$_2$ as a prime candidate axion insulator for topological antiferromagnetic spintronics applications.

axion insulator | magnetism | spin polarization | ARPES | topological surface states

Understanding the interplay between magnetism and high-order topology in a quantum material is currently one of the most challenging research directions in materials science, aiming at future spintronics applications (1, 2). Among exotic new quantum phases in three-dimensional (3D) magnetic topological insulators, a key element that enables many topological phase transitions is the breaking of time-reversal symmetry (TRS) induced by magnetic order; TRS breaking is the basis of the quantum anomalous Hall effect (3, 4) and of the topological magnetoelectric (TME) effect (4, 5). In the latter case, the mutual control of magnetic/electric polarization led to the theoretical prediction of a new quantum phenotype—the axion insulator—representing the condensed matter analog of the axion elementary particle postulated in high-energy physics by quantum chromodynamics (6). In its theoretical description, the magnetoelectric coupling term changes sign under TRS ($\mathcal{T}$) or inversion symmetry ($\mathcal{I}$), and the axion phase angle $\theta$ is quantized if either $\mathcal{T}$ or $\mathcal{I}$ is preserved (7). This translates in a topological classification defined by the $\mathbb{Z}_2$ index, where a nontrivial topology is protected by either $\mathcal{I}$ or $\mathcal{T}$. For centrosymmetric topological insulators a $\mathbb{Z}_4$ parity-based invariant is also defined; systems with $\mathbb{Z}_4 = 2$ host quantized TME effects, distinctive of an axion insulator (8–10).

Initial attempts to experimentally exploit the coexistence of magnetism and topology focus on hybrid systems based on proximity effects between magnetic layers and nonmagnetic topological insulator layers, or in hetero-tructures where magnetic topological insulators were obtained by chemical doping (11). In both approaches, however, the optimization and the control of magnetic/topological properties are difficult. The successful realization of bulk compounds, and in particular of antiferromagnetic topological insulators (AFI) (12), has recently been reported. Three-dimensional AFIs potentially satisfy many prerequisites for the axion insulator state, as they display a nontrivial topology characterized by a $\mathbb{Z}_2 = 1$ coupled to a magnetic layered structure with intraplane ferromagnetic order (2D ferromagnetism) and antiferromagnetic interplane coupling (3D A-type antiferromagnetism).

Relevant examples have been reported in the family of tetradymite-type ternary chalcogenides (13), with the most representative member being MnBi$_2$Te$_4$ (14). In this case, the A-type antiferromagnetism and the out-of-plane easy magnetization axis are due to the Mn atoms. The investigation of the interplay between topology and magnetism, a key property related to axion physics (15–18), is, however, lacking in this material, and in cases such as this, where the magnetic properties arise from the presence of Mn $3d$ electronic states, the magnetic character cannot be spectroscopically disentangled from the contribution of the $p$ electrons from Bi and Te.

Recently, an alternative platform for the realization of a 3D axion insulator has been established, using $4f$-electron-based lanthanides as magnetic dopants. Following theoretical predictions, the localized nature of $4f$ electrons may guarantee not only a clear distinction between electronic states but also a reduced hybridization of the magnetic and topological states, possibly resulting in a distinct control of magnetic and

## Significance

Understanding the mutual influence between magnetic and topological properties in a solid system is a fundamental challenge for quantum materials research. The so-called axion insulator is one such case, with exotic properties related to the magnetoelectric effect. In this work, by combining chemical and magnetic-state sensitive electron and X-ray spectroscopies with first-principle calculations we reveal that EuSn$_2$P$_2$ holds the characteristics of an axion insulator and displays "hidden" electronic properties arising from its layer-dependent ferromagnetic character. As a function of the termination, we observe specific electronic states, holding a spin arrangement representative of a topological insulator. Furthermore, the direction of magnetization enables topological protection, a key property related to axion-based physics.

PHYSICS

topological properties (8). To date, a few *f*-based magnetically ordered AFI candidates have been realized, namely EuIn$_2$As$_2$, EuSn$_2$As$_2$ and EuSn$_2$P$_2$ (19–23). EuIn$_2$As$_2$ and EuSn$_2$As$_2$ both have a $\mathbb{Z}_4 = 2$ invariant, i.e., a nontrivial topology (8, 19), yet a complete spectroscopic characterization with spin analysis for materials in this family is lacking.

Here we report a direct visualization of the spin texture and the topological character in EuSn$_2$P$_2$. We use chemically selective electron and X-ray spectroscopies with sensitivity to local and long-range magnetic order, supported by model calculations, to reveal the presence of both topological electronic states and in-plane 2D ferromagnetism. These electronic states are very distinct in energy and *k*-space, corresponding to a minimal hybridization of the Eu *4f* states with the Sn- and P-derived states. Below its T$_{\text{Néel}}$ of 30 K (22), spontaneous in-plane long-range magnetic order sets in arising from the Eu$^{2+}$ atoms only, and an extremely robust spin polarization with easy axis in the Eu plane is found, without applying any external magnetic field. Layer-dependent calculations reveal that in-plane ferromagnetic character is the origin of the strong topological protection observed in the system. We further observe surface states, clearly separated from the bulk states, corresponding to the specific P termination. Remarkably, spin-momentum locking of the P-derived surface electronic states is found below T$_{\text{Néel}}$, revealing that topology and magnetism coexist in a layer-dependent fashion and promoting EuSn$_2$P$_2$ as a 3D axion insulator. Our results reveal a richer physics than previously thought, confirming EuSn$_2$P$_2$ as a candidate system for future antiferromagnetic (AFM)-based spintronics applications and axionic topology.

## Results and Discussion

Single crystals of EuSn$_2$P$_2$ were grown using the Sn-flux method (22). EuSn$_2$P$_2$ crystallizes in a rhombohedral structure in which Eu atoms and the Sn-P hexagonal network form hexagonal layers and stack along the *c* direction, as shown in Fig. 1*A*, with the corresponding surface and bulk Brillouin zones presented in Fig. 1*B*. The space group of the lattice is $R\bar{3}m$ (No. 166) and the lattice is centrosymmetric. The crystal structure was determined by X-ray diffraction (see *SI Appendix*, Tables S1–S3), confirming the phase identity; topographic images obtained by scanning tunneling microscopy (see *SI Appendix*, Fig. S1) show that the cleaved surface is composed of large, homogeneous terraces, hundreds of nanometers wide, interrupted by steps. The step height corresponds to the distance between homonuclear layers, thus indicating that all terraces have the same atomic termination.

The angle-resolved photoemission spectroscopy (ARPES) characterization of the electronic states of EuSn$_2$P$_2$ compared to first-principle calculations is presented in Fig. 1. The symmetry-resolved theoretical bulk band structure along the $\bar{\Gamma} - \bar{K}$ and $\bar{\Gamma} - \bar{M}$ directions (left halves of Fig. 1 *C* and *D*) shows a very good agreement with the experimental E vs. *k* dispersion maps (Fig. 1 *E* and *F*) (22). Several dispersive features are experimentally observed (labeled as $\alpha$, $\beta$, $\gamma$, and $\delta$) and attributed through the calculations to the P and Sn bulk states, while the almost nondispersive $\zeta$ states, located at binding energy $\simeq -1.5$ eV, originate from the Eu *4f* orbitals, in excellent agreement with the calculations. Knowing that electronic states with weak overlap/hybridization favor spin unpairing, hence a localized magnetic character, this observation further corroborates the role of Eu as the magnetic driver in EuSn$_2$P$_2$. The calculations shown in Fig. 1 *C* and *D* indicate that the P *3p* bands ($\alpha$) display hole-like band dispersion close to the Fermi level. Remarkably, the linearly dispersing bands labeled $\sigma$ and *P*, observed in the experimental ARPES maps (highlighted in the enlarged views in Fig. 1 *G* and *H*), find no match with the bulk calculations. The *P* band can be reproduced in calculations only

when considering the phosphorous-terminated surface (right halves of Fig. 1 *C* and *D*). It appears clearly outside of the projected bulk band edge in the surface calculation. The $\sigma$ band, close to the bulk band edge, has no evident match, yet it can be identified as a surface resonance (24). The comparison between experiment and theory suggests that the $\sigma$ and *P* bands are surface states with main contribution from P *3p* orbitals.

The identification of extra bands as a specific feature of the P-terminated surface is made even clearer in Fig. 1*I*, where experimental isoenergetic Fermi surfaces for different terminations are shown compared to the P-terminated surface calculation. Horizontal cuts ($k_y = 0$ Å$^{-1}$) of the experimental data clearly highlight the presence of the "extra" $\sigma$ and *P* bands, the latter corresponding to a bright intense warped hexagon surrounding the bulk structure in the ($k_x - k_y$) plot. This intense P-derived band has a Fermi velocity of 3.24 eVxÅ ($4.92 \times 10^5$ m/s) and $k_F = 0.23$ Å$^{-1}$. Experimental Fermi surface measurements for the P-terminated surface at different photon energies are shown in *SI Appendix*, Fig. S5.

EuSn$_2$P$_2$, similarly to EuSn$_2$As$_2$ and EuIn$_2$As$_2$, is classified as an A-type antiferromagnet, as determined by theoretical predictions and bulk-sensitive magnetometric measurements (8, 20, 22). The *4f* electrons of Eu are tightly bound and preserve a localized character when passing from the atom to the solid, as indicated by the nondispersive $\zeta$ band in Fig. 1. The proximity of the *4f* levels to the Fermi energy may, however, lead to instabilities of the charge configuration of the Eu, i.e., valence fluctuations, which would have a strong impact on the ferromagnetic character of the material. In order to avoid ambiguity in the interpretation of the magnetic properties that might result from uncertainty of the Eu valence, we performed X-ray absorption spectroscopy (XAS) and X-ray magnetic circular dichroism (XMCD) in total yield mode [average probing depth 6 nm (25)] at the Eu $M_{4,5}$ edges. The lineshape of the XAS spectrum measured at 15 K (below T$_{\text{Néel}}$) is compared in Fig. 2*A* with theoretical calculations for the Eu$^{2+}$ and Eu$^{3+}$ valences (26), revealing that this material has a pure Eu$^{2+}$ character.

For a layered AFM system, one might expect an XMCD signal that averages to zero, due to opposite contributions of antiparallel layers of Eu spins. However, any such measurement averages the absorption spectrum over several layers, whose contributions are weighted by their proximity to the surface; a small XMCD signal is still detectable for that reason, whose shape is in excellent agreement with an Eu$^{2+}$ contribution (27). The measured XMCD in Fig. 2*B* is roughly two orders of magnitude smaller than the value expected for an isolated, fully saturated Eu moment if the atom is in a $4f^7(6s^2)$ configuration (Eu$^{2+}$, with a total spin S = 7/2) (21, 28). The small yet clear magnetic signal, which vanishes above T$_{\text{Néel}}$ (*SI Appendix*, Fig. S3), is measured without applying any external magnetic field, and testifies the presence of long-range magnetization in the bulk. Thus, these results confirm that layered antiferromagnetism (A-type) sets in spontaneously in EuSn$_2$P$_2$ when crossing T$_{\text{Néel}}$.

The small residual XMCD signal is compatible with both out-of-plane and in-plane magnetization of a single Eu layer due to the geometry of the experiment; insights into the layer-dependent electronic and magnetic properties are given in Fig. 2 *C* and *D* by vectorial spin-resolved ARPES results (29). ARPES probing depth is in the range of two Eu layers, i.e., much more sensitive to the magnetic signal of the topmost layer, taking into account the photon energy used and the large *c* lattice constant of the unit cell (the periodicity of the AFM order is $2c/3$, as sketched in Fig. 1*A*) (30). Indeed, a strong (up to 19%) spin polarization of Eu *4f* states along the *x* direction is observed below T$_{\text{Néel}}$, while along both the *y* direction and the *z* direction (see *SI Appendix*, Fig. S4) no magnetic signal is found. The in-plane magnetization appears below and disappears above T$_{\text{Néel}}$, in a reversible way. These results confirm that the
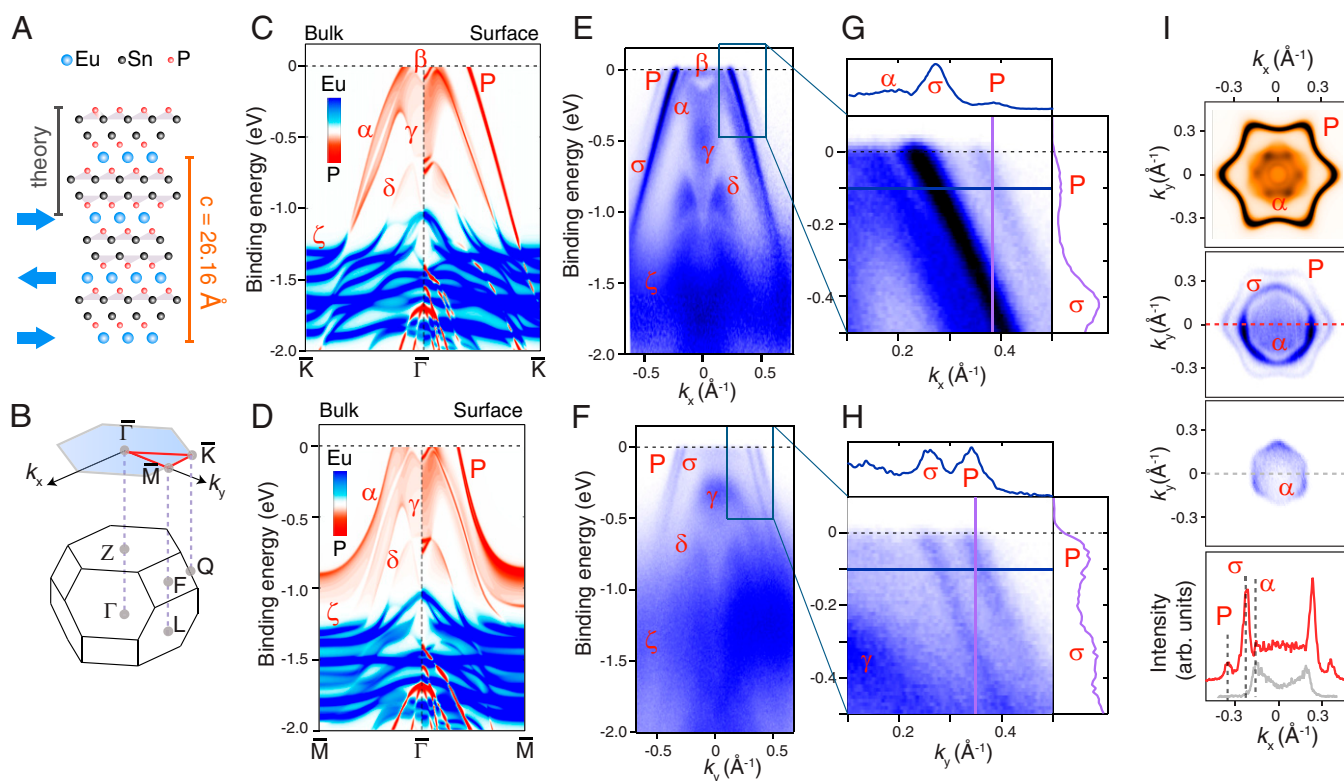
**Fig. 1.** Electronic structure of the EuSn$_2$P$_2$ (001) surface. (*A*) Hard sphere representation of the crystal and magnetic structure of EuSn$_2$P$_2$, with the A-type antiferromagnetic arrangement of Eu spins indicated by the arrows. The gray line indicates the extension of thickness corresponding to the surface calculation in *C* and *D*, whereas the orange line marks the extension of the vertical axis of the unit cell. (*B*) Bulk rhombohedral and corresponding 2D-projected hexagonal Brillouin zone with high symmetry lines, arising from the $R\bar{3}m$ symmetry space group. (*C* and *D*) Symmetry resolved theoretical bulk- (*Left*) and surface-only (*Right*) band structure, respectively in the $\bar{\Gamma} - \bar{K}$ and $\bar{\Gamma} - \bar{M}$ directions, showing the contribution of Eu and P. The position of the Fermi level has been fixed to match the experimentally measured one. Each surface state is plotted with a color corresponding to the integrated charge density of the state within the topmost two EuSn$_2$P$_2$ unit blocks as indicated in *A*. (*E* and *F*) ARPES maps along the $\bar{\Gamma} - \bar{K}$ and $\bar{\Gamma} - \bar{M}$ directions, measured at $h\nu = 27$ eV (respectively at T = 15 K and T = 80 K). (*G* and *H*) Magnified high-resolution maps of the dispersion near E$_F$; the extra bands ($\sigma$ and P) are highlighted. Momentum distribution curve (MDC) and EDC are the blue and purple solid lines, respectively, in the top and side panels. (*I*) From top to bottom: calculated $k_x - k_y$ isoenergetic Fermi surface for P-terminated surface; experimental $k_x - k_y$ isoenergetic Fermi surface maps for P-terminated ($h\nu = 27$ eV and T = 15 K) and non–P-terminated surface ($h\nu = 35$ eV and T = 77 K); experimental MDC cuts along $k_x$ axis ($\bar{\Gamma} - \bar{K}$ direction), corresponding to, respectively, red and gray dashed lines for the two different terminations, with the extra bands $\sigma$ and P indicated, as well as the $\alpha$ bulk band. The presence of different terminations has been verified by moving the light spot across the sample surface and monitoring changes of band structure around the Fermi level. The P termination was identified by comparison with calculations.

long-range magnetization is fully Eu-derived and aligns spontaneously to exhibit 2D ferromagnetism (in-plane ferromagnetic intralayer coupling). We stress that the presence of a robust magnetic signal in zero applied magnetic field is a prerequisite for axion-driven effects and antiferromagnetic spintronics application (15).

Having ascertained the nature of the long-range magnetization and the presence of strong local magnetic moment at the Eu-sites with pure Eu$^{2+}$ character, we now unravel the topological properties of EuSn$_2$P$_2$ in the presence of the in-plane AFM order. We have computed the $Z_4$ invariant, the $Z_2$ invariant, and the mirror Chern number (MCN) $n_M$. The parity-based higher-order $Z_4$ invariant is given by $Z_4 = \sum_{i=1}^{8} \sum_{n=1}^{n=occ} \frac{1 + \xi_n(\Gamma_i)}{2} mod\, 4$, where $\xi_n(\Gamma_i)$ is the parity eigenvalue (+1 or −1) of the $n$th band at the $i$th time-reversal invariant point $\Gamma_i$ and $n = occ$ is the number of occupied bands (31). The $Z_4$ invariant is well defined for an inversion symmetric system such as EuSn$_2$P$_2$, even in the absence of TRS. Our calculations show $Z_4 = 2$ with in-plane AFM, suggesting that EuSn$_2$P$_2$ is a 3D AFM axion insulator, with a quantized topological magnetoelectric effect (axion coupling $\theta = \pi$) (32, 33). Based on this result, one would expect that EuSn$_2$P$_2$ displays gapped surface states on all faces and gapless chiral hinge states between two gapped surfaces. Although

generally undefined in a system with broken TRS, $Z_2$ can be expanded to classify topological states in magnetic systems if the system possesses a specific magnetic configuration, for instance an AFI state, in which one defines the combined symmetry $S = \Theta T_{1/2}$, where $\Theta$ is the time-reversal operator and $T_{1/2}$ is the lattice translational symmetry of the crystal that is broken by the AFI order (12, 34). Under this definition, we calculated the $Z_2$ invariant by the Wilson loop method, resulting in a nontrivial $Z_2 = 1$ (see *SI Appendix*, Fig. S10*A*) (34). Next, we consider that EuSn$_2$P$_2$ in its AFI phase retains a mirror plane that is perpendicular to the in-plane magnetic moment, corresponding to a nontrivial MCN $n_M = 1$ on the $k_x = 0$ plane, indicating that EuSn$_2$P$_2$ is also a topological crystalline insulator.

The presence of both a nontrivial $Z_2$ and the MCN $n_M = 1$ has important consequences on the topology of the system. The extra mirror symmetry and $Z_2$ index induced by the in-plane magnetic order constitutes an additional and robust protection of the Dirac fermions. Such a symmetry preserves a gapless surface state on the side surface (010) around $\bar{\Gamma}$ and on the (001) surface along the $\bar{\Gamma} - \bar{M}$ direction (see *SI Appendix*, Figs. S9*C* and S10*D*) (19).

The effect of magnetic order is outlined in Fig. 3 *A* and *B*, which compare the spectral weights calculated for the (001) surface along the $\bar{\Gamma} - \bar{M}$ direction in both the nonmagnetic and
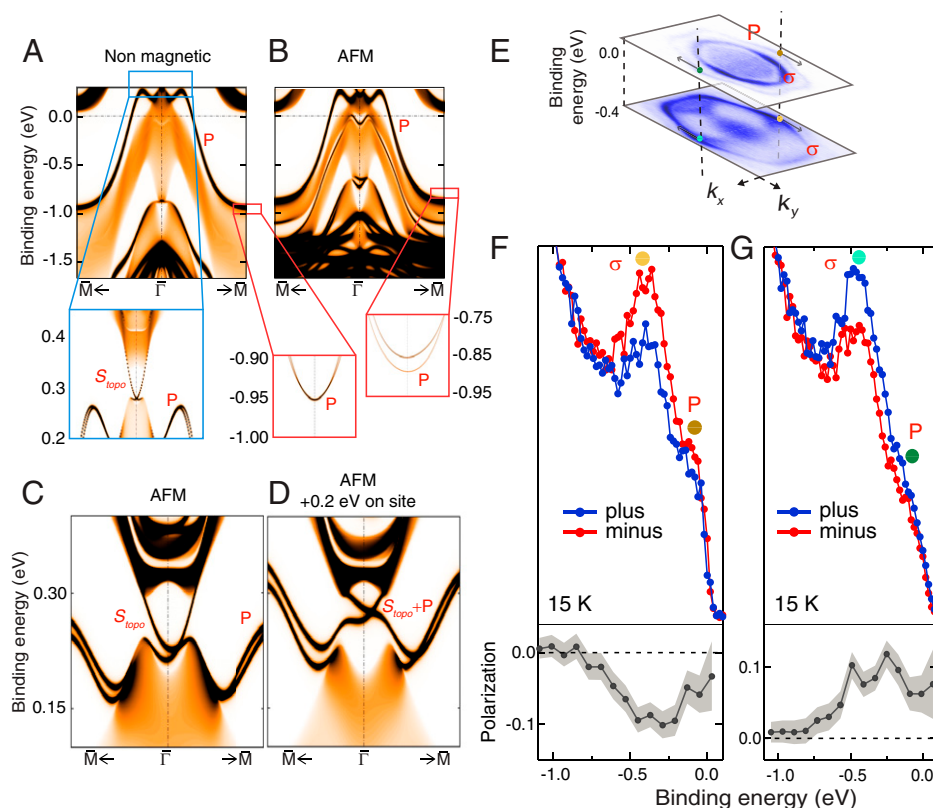
PHYSICS
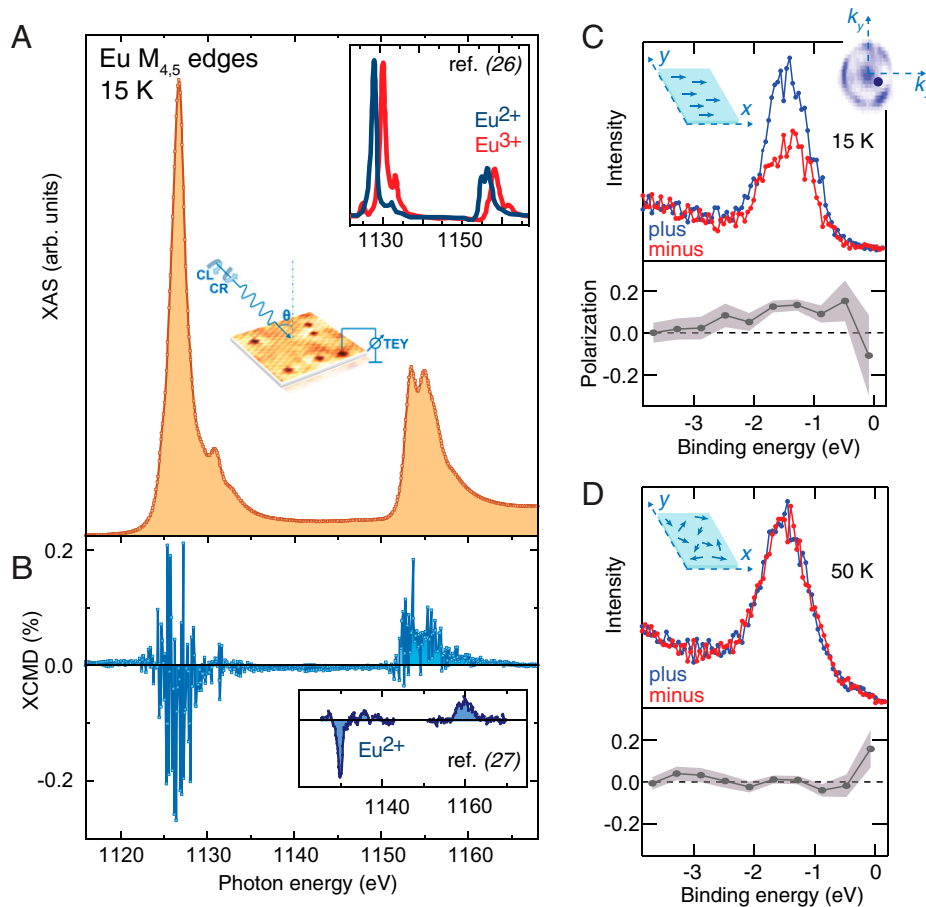
**Fig. 2.** Magnetic structure of the Eu layer. (*A*) Absorption spectrum of $EuSn_2P_2$ at the $M_{4,5}$ edges measured at T = 15 K, i.e., below $T_{Néel}$, summing circular right (CR) and circular left (CL) polarized spectra. (*Insets*) Scheme of the experimental geometry for the polarization-dependent XAS measured in the TEY mode and the theoretical spectra for $Eu^{2+}$ and $Eu^{3+}$ from ref. 26. (*B*) Normalized XMCD obtained as the difference between CR and CL spectra. (*Inset*) The experimental XMCD signal of $Eu^{2+}$ from ref. 27. (*C* and *D*) Spin-resolved EDCs of the Eu $4f$ core level measured at T = 15 K and T = 50 K, i.e., below and above the ordering $T_{Néel}$ temperature. Resulting spin polarization curves are shown in the lower panels. Spectra have been measured at $h\nu = 75$ eV, at the momentum value indicated as a dark-blue spot in the surface Brillouin zone shown in the top-right inset. The spin direction probed is along the $x$ axis, in the real-space reference frame represented in the top-left inset, which also illustrates the inferred direction of the Eu magnetic moments in the outer layer, since negligible spin polarization has been observed in the other real-space directions.

AFM configurations. The overall surface band structure does not change significantly, with the exception of the strong intensity from the Eu-derived states, absent in nonmagnetic calculation and centered around −1.5-eV binding energy (BE) in the AFM configuration, in good agreement with the ARPES characterization. The topological Dirac surface state ($S_{topo}$) is visible in the bulk gap at $\bar{\Gamma}$ in the nonmagnetic case at 0.28 eV above the Fermi level (light blue inset of Fig. 3*A*). The onset of magnetic order shifts the locus of the Dirac point in momentum space without opening a gap (Fig. 3*C*); the Dirac crossing position above the Fermi level curtails its direct observation by ARPES (14, 18). Other surface states around the bulk band gap are found both in nonmagnetic and AFM cases, labeled *P* since they correspond to the *P* band observed in ARPES. In the nonmagnetic case, these surface states are degenerate at $\bar{M}$ (Fig. 3*A*, red inset) and merge into the bulk valence band around $\bar{\Gamma}$ above the Fermi level. The broken TRS in the AFM phase opens a gap at $\bar{M}$ (Fig. 3*B*, red inset), not visible in the experiment due to the vanishing intensity at higher BE and to the overlap with other bulk bands. By applying to this calculation an on-site energy of 0.2 eV on the surface atoms to push up the energy position of the surface states (Fig. 3*D*), we find that the connectivity of the topological surface state changes dramatically (35, 36): $S_{topo}$ is no longer merged into the projected

bulk band around the $\bar{\Gamma}$ point as in Fig. 3*C* but connects with one of the *P* bands and forms a new surface band, labeled $S_{topo} + P$, which starts from bulk conduction band around $\bar{\Gamma}$, crosses the boundary of the BZ, and connects to the bulk valence band. As the surface on-site energy does not affect the bulk topology, the connectivity of surface state maintains its character. Therefore, the *P* band is part of a topological surface state.

Spin-ARPES results shown in Fig. 3 *F* and *G* provide clear spectroscopic evidence of the topological character of the P-derived states. Spin-ARPES energy distribution curve (EDC) spectra measured at T =15 K (i.e., below $T_{Néel}$) at two opposite momentum values display clear spin-momentum locking of the *P* band (as well as the surface resonance $\sigma$) with polarization inversion of the *y* component of the spin (sketch in Fig. 3*E*). The same spin inversion is also observed above $T_{Néel}$ (*SI Appendix*, Fig. S7). These results indicate that 1) the observed spin polarization has a nonmagnetic origin, 2) TRS is preserved as expected for a topological surface state (2, 23, 37, 38), and 3) the topological character is strong and not influenced by in-plane layered ferromagnetism, as opposed to what has been observed in $MnBi_2Te_4$ for the out-of-plane direction of the magnetization (14). As outlined above, calculations predict the presence of two split P bands, which should carry opposite spins. The splitting is so small that it cannot be resolved by the

Pierantozzi et al.
Evidence of magnetism-induced topological protection in the
axion insulator candidate $EuSn_2P_2$

**Fig. 3.** Topological spin texture of the P-derived electronic states. (*A* and *B*) Calculated surface spectral weight along the $\bar{\Gamma} - \bar{M}$ direction of the P-terminated surface of the (001) face in the nonmagnetic and AFM phases, respectively. (*Red Insets*) Enlarged views at $\bar{M}$ point for both configurations. (*Blue Inset*) Enlarged view of the region around the $\bar{\Gamma}$ point above Fermi level for the nonmagnetic case. (*C*) Enlarged view of the calculations in the AFM configuration in *B* around the $\bar{\Gamma}$ point above the Fermi level. (*D*) Same calculation as *C* with added surface on-site energy of 0.2 eV. (*E*) Experimental geometry of the spin-resolved ARPES measurement. EDCs are measured at $h\nu$ = 27 eV in two different $k$-space locations, indicated by the two vertical dashed lines cutting the constant-energy ARPES color maps. The two k-space points lie at opposite sides with respect to $\bar{\Gamma}$ point along the $k_x$ axis (i.e., along $\bar{K}' - \bar{\Gamma} - \bar{K}$ direction). The colored spots highlight that the two vertical cuts intersect the *P* band at the Fermi level and the $\sigma$ band at a binding energy of $-0.4$ eV, allowing a probe of the spin structure of both bands. The arrows show the direction of electron spins inferred from the spin-resolved measurements. (*F* and *G*) Spin-resolved EDCs and, in the lower panels, the resulting spin polarization, measured at 15 K (i.e., below $T_{Néel}$) in the two opposite momentum points illustrated by dashed lines in *B*. The color of the spots, gold and brown in *C* and light and dark green in *D*, help identify the corresponding energy-momentum positions in the band structure shown in *B*. The spatial direction of the spin probed in these measurements is along the *y* direction; for other directions see *SI Appendix*, Fig. S9.

energy and momentum resolutions of our system (30 meV and 0.01 Å$^{-1}$, respectively), yet the imbalance in the spin-projected weight of the two bands results in a net polarization of the photoemission signal, revealing their topological character.

Our theoretical and experimental observations provide clear evidence that EuSn$_2$P$_2$ has a termination-dependent surface electronic structure with multiple topology linked to the alignment of the Eu magnetic moments. In particular, our theoretical results predict the existence of gapless surface states protected by the combination of different nontrivial topological invariants, i.e., the inversion symmetry plus the presence of a mirror plane perpendicular to the magnetic moment. Our experimental results confirm this scenario, with the observation of spin-momentum locking of the P-derived surface states, coexisting with in-plane ferromagnetism. The observed extra topological protections in EuSn$_2$P$_2$ are expected to vanish when the mirror in-plane symmetry is broken, as for example in presence of an out-of-plane spin component. This symmetry-derived and termination-dependent link between topology and magnetism may open new routes in the realization of topological spintronics devices and in topological antiferromagnetic heterostructures.

## Materials and Methods

**Sample Growth and Characterization.** EuSn$_2$P$_2$ single crystals were obtained placing Eu chunks, red phosphorus, and Sn granules in an alumina crucible

with the molar ratio of 1.1:2:20. The crucible was sealed into an evacuated quartz tube which was then heated to 600 °C for 24 h and then underwent a second heat treatment at 1,050 °C. Successively, the tube was cooled down to 600 °C at a rate of 3 °C/h. When this temperature was reached, excess Sn was centrifuged out and shiny hexagonal single crystals (~1 × 1 × 0.1 mm³) were obtained. The samples were characterized by X-ray diffraction, using a Bruker Apex II diffractometer with Mo radiation ($\lambda_{K\alpha}$ = 0.710 73 Å); the results of the refinement (see ref. 22 for details) are displayed in *SI Appendix*, Tables S1–S3.

**Calculations.** We computed the electronic structures using the projector augmented wave method (39, 40) as implemented in the VASP package (41) within the generalized gradient approximation schemes (GGA) (42) and GGA plus Hubbard U (GGA + U) scheme (43). On-site U = 5.0 eV was used for Eu 4f orbitals. A 11 × 11 × 3 Monkhorst Pack k-point mesh was used in the computations. The spin-orbit coupling effects were included in calculations. The experimental lattice parameters were used. We used Eu f and d orbitals, Sn p orbitals, and P p orbitals to construct Wannier functions, without performing the procedure for maximizing localization (44). For the surface state calculation, we used the semiinfinite Green function approach.

**ARPES.** The crystals were cleaved in ultra-high-vacuum (UHV) condition inside the ARPES end-station installed on the low-energy branch of the APE beamline (APE-LE) (29) at Elettra synchrotron (Trieste, Italy). Such a chamber is equipped with a Scienta DA30 hemispherical electron analyzer (30° angular acceptance), which allows mapping the electronic bands over the extended areas of the Brillouin zone without sample rotation. ARPES experiments were performed at a base pressure <10$^{-10}$ mbar. The sample was cooled down to 15 K with a continuous flow cryostat. The incidence angle of synchrotron

radiation was 45°. Linear p-polarized radiation has been used. When not otherwise specified, the overall energy resolution was set to ~30 meV, and the angular resolution was set to 0.2° (corresponding to ~0.01 Å$^{-1}$ at the used photon energy), with a spot size of roughly 100 μm ×100 μm.

**XAS and XMCD.** Soft XAS and XMCD spectroscopy experiments were performed at the Soft X-Ray branch of I09 beamline (45) at the Diamond Light Source Ltd. (Didcot, United Kingdom). The crystals used in this part of the experiment came from the same batch as ARPES measurements and were cleaved in UHV condition. Samples were shined with circularly polarized light in a range of photon energies between $h\nu = 1{,}115$ eV and $h\nu = 1{,}170$ eV. A grazing incidence geometry has been used (i.e., 30° angle between the X-ray beam and the surface normal) resulting in a focused beam spot of 40 μm × 20 μm in size. The spectra were taken in total electron yield (TEY), normalizing the intensity of the sample current to the incident photon flux at each energy value. The measurements were taken at T = 15 K, i.e., below T$_{Néel}$. The XMCD is given by the difference between the two circular polarizations, right (CR) and left (CL) at remanence, with no external magnetic field applied to the sample.

**Scanning Tunneling Microscopy and Spectroscopy.** Scanning tunneling microscopy (STM) topography images and Scanning Tunneling Spectroscopy dI/dV characteristics were collected with a commercial Omicron Low-Temperature STM operating in UHV with liquid nitrogen cryostat (77 K, base pressure < 8 × 10$^{-11}$ mbar). The microscope is connected to a UHV preparation chamber equipped with a dedicated stage for mechanical cleavage of samples at room temperature. At the moment of cleavage, the base pressure of the stage was 1.3 × 10$^{-8}$ mbar. The sample was then immediately transferred to the low-pressure stage (2 × 10$^{-9}$ mbar) and after 2 min was moved in the STM, where it was cooled. The STM electronics is interfaced with a lock-in amplifier for the first derivative measurements. Lock-in parameters: amplitude 16 mV, frequency 978.5 Hz, time constant 3 ms, time raster 150 ms/point, acquisition delay 90 ms.

**Data Availability.** All study data are included in the article and/or *SI Appendix*.

1. M. Gibertini, M. Koperski, A. F. Morpurgo, K. S. Novoselov, Magnetic 2D materials and heterostructures. *Nat. Nanotechnol.* **14**, 408–419 (2019).
2. Y. Tokura, K. Yasuda, A. Tsukazaki, Magnetic topological insulators. *Nat. Rev. Phys.* **1**, 126–143 (2019).
3. R. Yu et al., Quantized anomalous hall effect in magnetic topological insulators. *Science* **329**, 61–64 (2010).
4. G. Xu, H. Weng, Z. Wang, X. Dai, Z. Fang, Chern semimetal and the quantized anomalous Hall effect in HgCr2Se4. *Phys. Rev. Lett.* **107**, 186806 (2011).
5. A. M. Essin, J. E. Moore, D. Vanderbilt, Magnetoelectric polarizability and axion electrodynamics in crystalline insulators. *Phys. Rev. Lett.* **102**, 146805 (2009).
6. N. P. Armitage, L. Wu, On the matter of topological insulators as magnetoelectrics. *SciPost Phys.* **6**, 1–35 (2019).
7. N. Varnava, D. Vanderbilt, Surfaces of axion insulators. *Phys. Rev. B* **98**, 245117 (2018).
8. Y. Xu, Z. Song, Z. Wang, H. Weng, X. Dai, Higher-order topology of the axion insulator EuIn_2As_2. *Phys. Rev. Lett.* **122**, 256402 (2019).
9. M. S. Bahramy, B. J. Yang, R. Arita, N. Nagaosa, Emergence of non-centrosymmetric topological insulating phase in BiTeI under pressure. *Nat. Commun.* **3**, 679 (2012).
10. L. Fu, C. L. Kane, Topological insulators with inversion symmetry. *Phys. Rev. B Condens. Matter Mater. Phys.* **76**, 045302 (2007).
11. Y. Hou, R. Wu, Axion insulator state in a ferromagnet/topological insulator/antiferromagnet heterostructure. *Nano Lett.* **19**, 2472–2477 (2019).
12. R. S. K. Mong, A. M. Essin, J. E. Moore, Antiferromagnetic topological insulators. *Phys. Rev. B Condens. Matter Mater. Phys.* **81**, 245209 (2010).
13. J. Li et al., Intrinsic magnetic topological insulators in van der Waals layered MnBi$_2$Te$_4$-family materials. *Sci. Adv.* **5**, eaaw5685 (2019).
14. M. M. Otrokov et al., Prediction and observation of an antiferromagnetic topological insulator. *Nature* **576**, 416–422 (2019).
15. C. Liu et al., Robust axion insulator and Chern insulator phases in a two-dimensional antiferromagnetic topological insulator. *Nat. Mater.* **19**, 522–527 (2020).
16. X. Wu et al., Distinct topological surface states on the two terminations of MnBi4Te7. *Phys. Rev. X* **10**, 031013 (2020).
17. Y. J. Chen et al., Topological electronic structure and its temperature evolution in antiferromagnetic topological insulator MnBi2Te4. *Phys. Rev. X* **9**, 041040 (2019).
18. Y. J. Hao et al., Gapless surface dirac cone in antiferromagnetic topological insulator MnBi2Te4. *Phys. Rev. X* **9**, 041038 (2019).
19. H. Li et al., Dirac surface states in intrinsic magnetic topological insulators EuSn2As2 and MnBi2nTe3n+1. *Phys. Rev. X* **9**, 041039 (2019).
20. H. C. Chen et al., Negative magnetoresistance in antiferromagnetic topological insulator EuSn2As2*. *Chin. Phys. Lett.* **37**, 047201 (2020).
21. M. Q. Arguilla et al., EuSn2As2: An exfoliatable magnetic layered Zintl-Klemm phase. *Inorg. Chem. Front.* **4**, 378–386 (2017).
22. X. Gui et al., A new magnetic topological quantum material candidate by design. *ACS Cent. Sci.* **5**, 900–910 (2019).
23. T. Sato et al., Signature of band inversion in the antiferromagnetic phase of axion insulator candidate EuIn2As2. *Phys. Rev. Res.* **2**, 033342 (2020).
24. C. Jozwiak et al., Spin-polarized surface resonances accompanying topological surface state formation. *Nat. Commun.* **7**, 13143 (2016).
25. B. H. Frazer, B. Gilbert, B. R. Sonderegger, G. De Stasio, The probing depth of total electron yield in the sub-keV range: TEY-XAS and X-PEEM. *Surf. Sci.* **537**, 161–167 (2003).
26. B. T. Thole, et al., 3d x-ray-absorption lines and the 3d94fn+1 multiplets of the lanthanides. *Phys. Rev. B Condens. Matter* **32**, 5107–5118 (1985).
27. B. J. Ruck et al., Magnetic state of EuN: X-ray magnetic circular dichroism at the Eu M 4,5 and L 2,3 absorption edges. *Phys. Rev. B Condens. Matter Mater. Phys.* **83**, 174404 (2011).
28. T. Kawamoto et al., Ferromagnetic amorphous oxides in the EuO-TiO2 system studied by the Faraday effect in the visible region and the x-ray magnetic circular dichroism at the Eu M4,5 and L2,3 edges. *Phys. Rev. B Condens. Matter Mater. Phys.* **88**, 024405 (2013).
29. C. Bigi et al., Very efficient spin polarization analysis (VESPA): New exchange scattering-based setup for spin-resolved ARPES at APE-NFFA beamline at Elettra. *J. Synchrotron Radiat.* **24**, 750–756 (2017).
30. P. D. C. King, S. Picozzi, R. G. Egdell, G. Panaccione, Angle, spin, and depth resolved photoelectron spectroscopy on quantum materials. *Chem. Rev.* **121**, 2816–2856 (2021).
31. A. M. Turner, Y. Zhang, R. S. K. Mong, A. Vishwanath, Quantized response and topology of magnetic insulators with inversion symmetry. *Phys. Rev. B Condens. Matter Mater. Phys.* **85**, 165120 (2012).
32. B. J. Wieder et al., Strong and fragile topological Dirac semimetals with higher-order Fermi arcs. *Nat. Commun.* **11**, 627 (2020).
33. C. Hu et al., Realization of an intrinsic ferromagnetic topological state in MnBi$_8$Te$_{13}$. *Sci. Adv.* **6**, eaba4275 (2020).
34. R. Yu, X. L. Qi, A. Bernevig, Z. Fang, X. Dai, Equivalent expression of Z2 topological invariant for band insulators using the non-Abelian Berry connection. *Phys. Rev. B Condens. Matter Mater. Phys.* **84**, 075119 (2011).
35. T. R. Chang et al., Prediction of an arc-tunable Weyl Fermion metallic state in Mo(x)W(1-x)Te2. *Nat. Commun.* **7**, 10639 (2016).
36. T. R. Chang et al., Band topology of bismuth quantum films. *Crystals (Basel)* **9**, 510 (2019).
37. Y. S. Hou, J. W. Kim, R. Q. Wu, Axion insulator state in ferromagnetically ordered CrI3/Bi2Se3/MnBi2Se4 heterostructures. *Phys. Rev. B* **101**, 121401(R) (2020).
38. Y. Tokura, M. Kawasaki, N. Nagaosa, Emergent functions of quantum materials. *Nat. Phys.* **13**, 1056–1068 (2017).
39. P. E. Blöchl, Projector augmented-wave method. *Phys. Rev. B Condens. Matter* **50**, 17953–17979 (1994).
40. G. Kresse, D. Joubert, From ultrasoft pseudopotentials to the projector augmented-wave method. *Phys. Rev. B Condens. Matter Mater. Phys.* **59**, 1758–1775 (1999).
41. G. Kresse, J. Furthmüller, Efficiency of ab-initio total energy calculations for metals and semiconductors using a plane-wave basis set. *Comput. Mater. Sci.* **6**, 15–50 (1996).
42. J. P. Perdew, K. Burke, M. Ernzerhof, Generalized gradient approximation made simple. *Phys. Rev. Lett.* **77**, 3865–3868 (1996).
43. S. L. Dudarev, G. A. Botton, S. Y. Savrasov, C. J. Humphreys, A. P. Sutton, Electron-energy-loss spectra and the structural stability of nickel oxide: An LSDA+U study. *Phys. Rev. B Condens. Matter Mater. Phys.* **57**, 1505–1509 (1998).
44. N. Marzari, D. Vanderbilt, Maximally localized generalized Wannier functions for composite energy bands. *Phys. Rev. B Condens. Matter Mater. Phys.* **56**, 12847–12865 (1997).
45. T. L. Lee, D. A. Duncan, A two-color beamline for electron spectroscopies at Diamond Light Source. *Synchrotron Radiat. News* **31**, 16–22 (2018).

**6 of 6** | **PNAS**
https://doi.org/10.1073/pnas.2116575119

Pierantozzi et al.
Evidence of magnetism-induced topological protection in the axion insulator candidate EuSn$_2$P$_2$